



UNIVERSIDADE ESTADUAL DE CAMPINAS
SISTEMA DE BIBLIOTECAS DA UNICAMP
REPOSITÓRIO DA PRODUÇÃO CIENTÍFICA E INTELLECTUAL DA UNICAMP

Versão do arquivo anexado / Version of attached file:

Versão do Editor / Published Version

Mais informações no site da editora / Further information on publisher's website:

<https://www.sciencedirect.com/science/article/pii/S0264127517310869>

DOI: 10.1016/j.matdes.2017.11.055

Direitos autorais / Publisher's copyright statement:

©2018 by Elsevier. All rights reserved.

DIRETORIA DE TRATAMENTO DA INFORMAÇÃO

Cidade Universitária Zeferino Vaz Barão Geraldo

CEP 13083-970 – Campinas SP

Fone: (19) 3521-6493

<http://www.repositorio.unicamp.br>



Compositional analysis on the reverted austenite and tempered martensite in a Ti-stabilized supermartensitic stainless steel: Segregation, partitioning and carbide precipitation☆

J.D. Escobar^{a,b,c}, J.D. Poplawsky^d, G.A. Faria^c, J. Rodriguez^a, J.P. Oliveira^c, C.A.F. Salvador^b, P.R. Mei^b, S.S. Babu^{e,f}, A.J. Ramirez^{c,*}

^a Brazilian Nanotechnology National Laboratory - LNNano - CNPEM, Campinas, SP, Brazil, 13083-970

^b College of Mechanical Engineering, University of Campinas – FEM - Unicamp, Campinas, SP 13083-860, Brazil

^c Welding Engineering, Department of Materials Science and Engineering, The Ohio State University, 1248 Arthur E. Adams Drive, Columbus, OH 43221, USA

^d The Center for Nanophase Materials Sciences, Oak Ridge, National Laboratory, USA, 37831

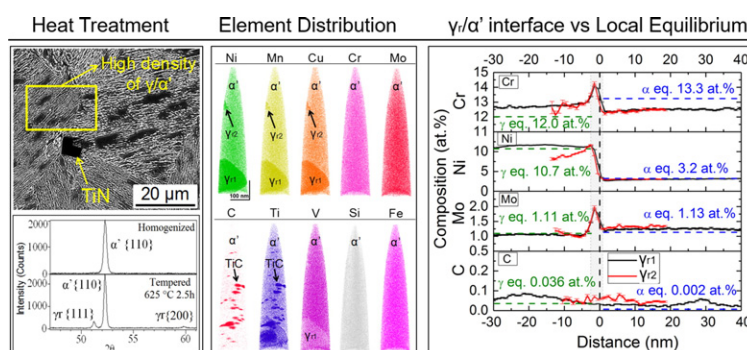
^e Mechanical, Aerospace and Biomedical Engineering, University of Tennessee, Knoxville, TN, USA, 37996-2210

^f Manufacturing Demonstration Facility, Oak Ridge National Laboratory, Knoxville, TN, USA

HIGHLIGHTS

- Austenite growth occurred by strong partitioning of Ni according to local equilibrium.
- Reverted austenite/martensite interface segregation of Cr, Mo, Si and Ti was evidenced.
- Virtually carbon-free reverted austenite and martensite were found after tempering due to precipitation of Ti (C, N).

GRAPHICAL ABSTRACT



ARTICLE INFO

Article history:

Received 7 June 2017

Received in revised form 22 October 2017

Accepted 24 November 2017

Available online 26 November 2017

Keywords:

Atom probe tomography

Austenite reversion

ABSTRACT

Controlling the amount of reverted austenite at room temperature allows for tailoring of mechanical properties in supermartensitic stainless steels. The austenite reversion and stabilization occurs during inter-critical tempering through partitioning of austenite-stabilizing elements. The degree of partitioning greatly depends on the reversion temperature, which dictates the local equilibrium conditions. Atom probe tomography and energy dispersive spectroscopy in transmission electron microscopy were used to study the austenite reversion mechanism in terms of the elemental distribution of austenite-stabilizing, ferrite-stabilizing and carbide forming elements. Synchrotron X-ray diffraction confirmed that the austenite equilibrium phase fraction was reached after 2.5 h of isothermal reversion at 625 °C, allowing for direct comparison with thermodynamic and kinetic

Abbreviations: α , ferrite in thermodynamic equilibrium; α' , tempered martensite; γ , austenite in thermodynamic equilibrium; γ_r , reverted austenite stabilized at room temperature; APT, atom probe tomography; XEDS, energy dispersive X-ray spectroscopy; ICT, inter-critical tempering; MCN, used to refer to titanium carbo-nitride precipitates; SMSS, supermartensitic stainless steels; SXRD, synchrotron X-ray diffraction.

☆ This manuscript has been authored by UT-Battelle, LLC under Contract No. DE-AC05-00OR22725 with the U.S. Department of Energy. The United States Government retains and the publisher, by accepting the article for publication, acknowledges that the United States Government retains a non-exclusive, paid-up, irrevocable, world-wide license to publish or reproduce the published form of this manuscript, or allow others to do so, for United States Government purposes. The Department of Energy will provide public access to these results of federally sponsored research in accordance with the DOE Public Access Plan (<http://energy.gov/downloads/doe-public-access-plan>).

* Corresponding author.

E-mail address: ramirezlondono.1@osu.edu (A.J. Ramirez).

calculations. However, such soaking time was not enough to produce compositional homogenization in the reverted austenite. The austenite reversion and stabilization mechanism was related mainly to strong partitioning of Ni. Negligible partitioning of Cr, Mo, Si and Ti were observed. Instead, these elements were strongly segregated at the reverted austenite/martensite interfaces. Carbon and Ti played a secondary role in the austenite stabilization through the precipitation of nano-sized Ti (C,N) with partial substitution of Ti by Mo. Virtually carbon-free austenite and martensite were observed away from the interfaces and precipitates.

© 2017 Elsevier Ltd. All rights reserved.

1. Introduction

The ability to tailor the mechanical properties through austenite reversion during inter-critical tempering (ICT) makes Supermartensitic Stainless Steels (SMSS) very interesting for applications in the oil and gas industry. Yield strength, work hardening, impact toughness and hardness can be modified by small variations in the volume fraction of reverted austenite stabilized at room temperature (γ_r) [1–6]. This behavior has been associated to Transformation Induced Plasticity (TRIP) effect [7–10].

The γ_r stabilization is a diffusion-controlled process, involving the mobility of γ -stabilizing elements, such as Ni and Mn, from the tempered martensite (α') matrix into the austenite [11–16]. Typically, after a couple of hours of isothermal reversion of SMSS at 625 °C, a tempered α' matrix with 10 to 20% volume of γ_r can be obtained [17–22]. Higher austenite thermal stability can be achieved through slow isothermal reversion kinetics at the lower portion of the γ/α ICT region [23]. This is due to a combined effect of strong partitioning of Ni [15, 19,21,24,25] into the austenite, and to the refined lath-like γ_r morphology achieved [6,21,26–29].

Atom Probe Tomography (APT) compositional analyses have been successfully conducted to understand the austenite stabilization through C partitioning in carbon steels [30–32], 13%Cr martensitic stainless steels [16], and through Mn partitioning in medium and high Manganese steels [11–13,33]. However, few APT studies have been published regarding the characterization of the austenite reversion mechanism in SMSS [15]. Although it has been stated that Ni is the main element affecting the austenite stabilization process in SMSS, these results are mainly referred to bulk measurements through transmission electron microscopy (TEM) [15,19,21]. The role of ferrite-stabilizing elements, such as Cr and Mo is even more difficult to quantify due to small partitioning and sharp interface segregation [14,15]. Besides, the direct quantification of the effect of interstitial elements such as C and N is challenging. Indirect methods, such as lattice parameter analysis, have been used to estimate the C content in reverted austenite [34]. However, these calculations are unreliable for stainless steels containing stabilizing elements such as Ti, Nb and V due to C capturing from the solid solution [14,27] through precipitation of Ti (C, N), which is the situation presented in this investigation.

In this work, the mechanisms of austenite reversion and stabilization were studied after an ICT cycle at 625 °C for 2.5 h, which is commonly used to produce a balanced microstructure with low hardness and high impact toughness in the production of pipelines for the oil and gas industry [1–6]. Through the suppression of retained austenite, we isolate a specific mechanism of austenite reversion, based on the isothermal nucleation and growth of austenite at the α'/α' laths. The elemental distribution of austenite-stabilizing, ferrite-stabilizing and carbide forming elements across the γ_r/α' interfaces was clarified via APT and energy dispersive X-ray spectroscopy (XEDS) using scanning transmission electron microscopy (STEM). Synchrotron X-ray diffraction (SXRD) allowed the tracking of the $\alpha' \rightarrow \gamma$ reversion kinetics during the ICT cycle. Both transformation kinetics and compositional results were interpreted with the aid of Calphad-based thermodynamic and kinetic calculations. The role of carbide precipitation and the elemental distribution across the matrix/Ti(C, N) interfaces was also addressed. The aim of this paper is to provide a better understanding of the role

of the alloying elements at the micro and nano scales, related to a well-known mechanical behavior obtained after inter-critical tempering.

2. Experimental

Samples from a hot rolled and annealed UNS S41426 Ti-stabilized SMSS were extracted and subjected to homogenization heat treatment in a tubular furnace at 950 °C for 20 min, followed by an ICT cycle at 625 °C for 2.5 h. Heating and cooling rates of $0.167 \text{ }^\circ\text{C}\cdot\text{s}^{-1}$ were used. A constant argon flux was maintained to prevent oxidation and decarburization. The nominal composition of the SMSS in atomic and weight percent is given in Table 1.

In situ X-ray diffraction measurements were conducted additionally in order to clarify the austenite transformation kinetics and the austenite thermal stability associated to the specific furnace tempering parameters aforementioned. This analysis was performed at the X-Ray scattering and thermomechanical simulation experimental station (XTMS), at the Brazilian National Synchrotron Source (LNLS). A thermomechanical simulator (Gleeble® 3550) coupled to the synchrotron light source allowed time-resolved tracking of the austenite transformation kinetics during the ICT cycle. A heating rate of $0.166 \text{ }^\circ\text{C}\cdot\text{s}^{-1}$ was used. The cooling process was conducted at $5 \text{ }^\circ\text{C}\cdot\text{s}^{-1}$ to simulate air quenching conditions. A linear detector, with 0.008° angular resolution was used to collect diffraction data from a partial spectra region including the {111} and {200} γ peaks and {110} α' peak. However, high and room temperature quantification was also performed including the {111}, {200}, {220}, {311}, and {222} γ peaks, and the {110}, {200}, {211}, and {220} α' peaks. Incident beam energy of 12 keV was used. A more detailed description of the quantification method can be found in [23,35]. Under the conditions used in the experiment, the uncertainty on the measured volume fraction of austenite ranges from 0.005 to 0.015 [23]. Therefore, error bars are not included in the figures.

Microhardness measurements were performed using a LECO M-400-H1 microhardness Vickers tester. Twenty indents using 200 g load, 200 μm step size and 15 s dwell time were performed. The average results, before and after IC tempering, are presented.

Atom probe tomography was used to characterize the compositional profile of the γ_r , α' and carbides, after furnace IC tempering. Site-specific focused ion beam (FIB) lift-outs were taken from regions with a high density of γ_r/α' interfaces. The size and distance between γ_r was approximately 200 and 500 nm, respectively. Regions of interest were annularly milled and cleaned with an ion beam to make needle shaped specimens suitable for field evaporation. The analyses were performed using a CAMECA Instruments LEAP® 4000 \times HR local electrode atom probe. The specimens were field evaporated in laser mode with a 200 kHz pulse repetition rate, 30 K specimen temperature, 100 pJ laser power, and a 0.5–1.0% detection rate. The resulting data was reconstructed and analyzed using the CAMECA IVAS software.

Table 1
Nominal composition of a Ti-stabilized SMSS.

| | C | N | Si | Mn | Ni | Cr | Mo | Cu | Ti | V |
|------|-------|--------|-------|-------|------|-------|------|------|-------|-------|
| wt% | 0.024 | 0.0129 | 0.260 | 0.480 | 5.90 | 12.02 | 1.93 | 0.09 | 0.130 | 0.040 |
| at.% | 0.111 | 0.0513 | 0.516 | 0.487 | 5.60 | 12.88 | 1.13 | 0.08 | 0.153 | 0.044 |

Deconvolution of the ions within overlapping isobars of different elements (e.g., Cr₅₄/Fe₅₄) was performed based on the natural abundances of the elements. The measured APT compositional profiles display error bars that were calculated according to Eq. 1, where s is the standard error assuming a random solid solution, c_i is the atomic concentration of a solute, and n_t is the total number of ions collected:

$$s = \sqrt{\frac{c_i(1-c_i)}{n_t}} \quad (1) \quad [36]$$

Energy Dispersive X-ray Spectroscopy measurements were performed in a 200 kV FEI Tecnai F20 Scanning Transmission Electron Microscope. Thin foils were prepared using site-specific FIB lift-out technique in regions containing a high density of γ_r/α' interfaces. Fig. 1 depicts two regions of interest containing precipitates (A) and γ_r/α' interfaces (B). These regions provided further compositional information, which was compared to the APT measurements.

Thermodynamic equilibrium calculations were conducted using Thermo-Calc software and TCFE9 database. The measured XEDS-STEM and APT compositional profiles were compared to the equilibrium calculations for a thermodynamic system allowing the precipitation of BCC (ferrite) and FCC (austenite and MCN) phases only. The calculations were performed using the SMSS nominal composition from Table 1, at the ICT temperature of 625 °C. For comparison purposes, a second set of thermodynamic calculations was also performed while allowing all possible phases to precipitate (ferrite, austenite, χ , σ , MCN, M₆C, M₂₃C₆, among others), relative to the same nominal composition.

Kinetic calculations were performed using DICTRA® to simulate the austenite growth during the ICT cycle. The simulation was set up in a planar geometry with a fully implicit scheme. The grid was created with 100 points and a width of 250 nm, which correlates with half of the average distance between clusters of reverted intra-granular austenite laths, with a point distribution geometrically biased towards zero. The BCC phase was set in all grid points with a constant composition distribution of 12.8 at.% Cr, 5.6 at.% Ni, 1.1 at.% Mo, 0.5 at.% Mn and Fe as a balance. At the zero position, an inactive FCC phase was introduced, requiring a minimum driving force of 10^{-5} J·mol⁻¹ to be activated. When activated, the region with the FCC phase had an initial size of 0.1 nm [37]. Activation happened at the earliest time step, at 10^{-7} s. A DICTRA® built-in dislocation assisted diffusion model was used to enhance the mobility, using dislocation densities for austenite (0.75×10^{14} m⁻²) and martensite (2×10^{14} m⁻²), consistent with

observed values for SMSS [38]. Burger's vectors were set as 2.51 and 2.55 Å for martensite and austenite, respectively, following lattice parameters measured on the peaks used to derive the austenite transformation kinetics. The energy fraction term was set to 0.68 for both phases, which is in good agreement with other research works [39]. The model was run at 625 °C for up to 2.5 h (9000 s). Phase information and elemental mobility values were retrieved from TCFE9 and MOBFE3 databases.

3. Results

3.1. Austenite reversion kinetics

Fig. 2a and b show the microstructure before and after tempering, respectively. After homogenization at 950 °C for 20 min, fresh lath martensite with no presence of δ -ferrite or retained austenite was obtained. After furnace tempering, 0.19 γ_r volume fraction was observed. This was evidenced by conventional XRD analysis, shown in Fig. 2c. A drop in hardness from 308 ± 7 HV_{200/15} to 286 ± 6 HV_{200/15} was observed after tempering. Fig. 2d shows XEDS results after homogenization, evidencing typical titanium nitrides (TiN) with sharp angular shapes [40–42]. Most of the precipitation of stable titanium nitrides (TiN) is expected to occur during the solidification process. These are not the focus of this investigation. However, such precipitates can easily be differentiated by their micrometric size and angular shapes.

Fig. 3 shows the results from austenite reversion kinetics during the reproduced time-resolved ICT cycle. During the heating stage, no austenite reversion was observed. The isothermal transformation started right after reaching the soaking temperature, evolving from 0 to 0.31 austenite volumetric fraction after 2.5 h. According to thermodynamic calculations, high temperature equilibrium was reached, corresponding to 0.32 volumetric fraction of austenite at 625 °C. Nevertheless, partial martensitic transformation occurred upon cooling, resulting in a total stable fraction of 0.18 γ_r at room temperature.

A more accurate quantification of the γ_r volumetric fraction at high and room temperature was performed using extended diffraction spectra. Despite the differences in cooling rate, a similar γ_r volume fraction was obtained at room temperature. The results are shown in Table 2.

3.2. Nano-scale compositional characterization

3.2.1. Reverted austenite/tempered martensite interface

Fig. 4a shows the APT reconstruction for the most representative alloying elements of the sample after the ICT cycle. Two γ_r laths at the bottom and at the top part of the tip were identified and labeled as γ_{r1} and γ_{r2} , respectively. It was evidenced that the γ -stabilizing elements, such as Ni, Mn and Cu, were preferentially partitioned into the γ_r . On the other hand, the α -stabilizing elements, such as Cr, Mo and Si showed a more homogeneous distribution. Precipitation of titanium carbides (TiC) was identified by the clustering of Ti and C atoms inside both martensitic and austenitic matrixes. Nevertheless, these precipitates were associated to titanium carbonitrides, or Ti (C, N), as discussed later in Section 4.3. A higher concentration of Ti was observed at the core of the γ_{r1} lath. This is not related to a Ti carbide, since there is no presence of C in the same region.

Fig. 4b depicts two γ_r/α' interfaces highlighted in dark green by a 6 at.% Ni isoconcentration surface, and a series of Ti carbides contoured in red by 30 at.% Ti + C isoconcentration surfaces. A high density of precipitates was observed at and near the γ_{r1}/α' interface. Smaller precipitates were observed in the proximities of the γ_{r2}/α' interface. This can be observed in more detail in Fig. 4c and d, respectively. The solute distribution across the γ_{r1}/α' and γ_{r2}/α' interfaces is summarized in Fig. 5 (for Fe, Cr, Ni, Mo and Mn) and Fig. 6 (for Ti, C, Cu, Si and V), which display proximity histograms of the 6 at.% Ni isoconcentration surfaces. Note that the 0 value in the distance axis does not necessarily correlate to the exact position of the interface. As there is a compositional

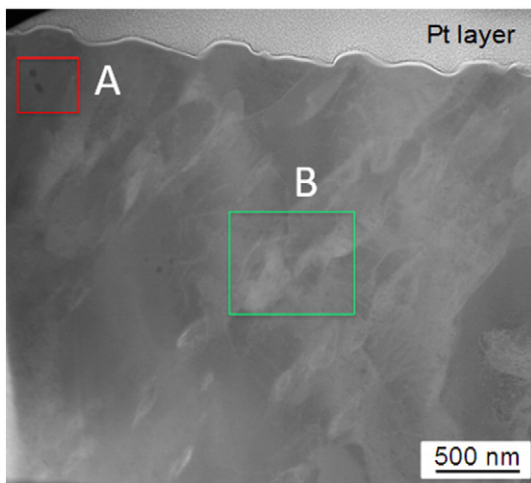


Fig. 1. STEM HAADF (High Angle Annular Dark Field) image of a thin foil prepared by site-specific FIB lift-out technique. Regions A and B contain precipitates and γ_r/α' interfaces, respectively.

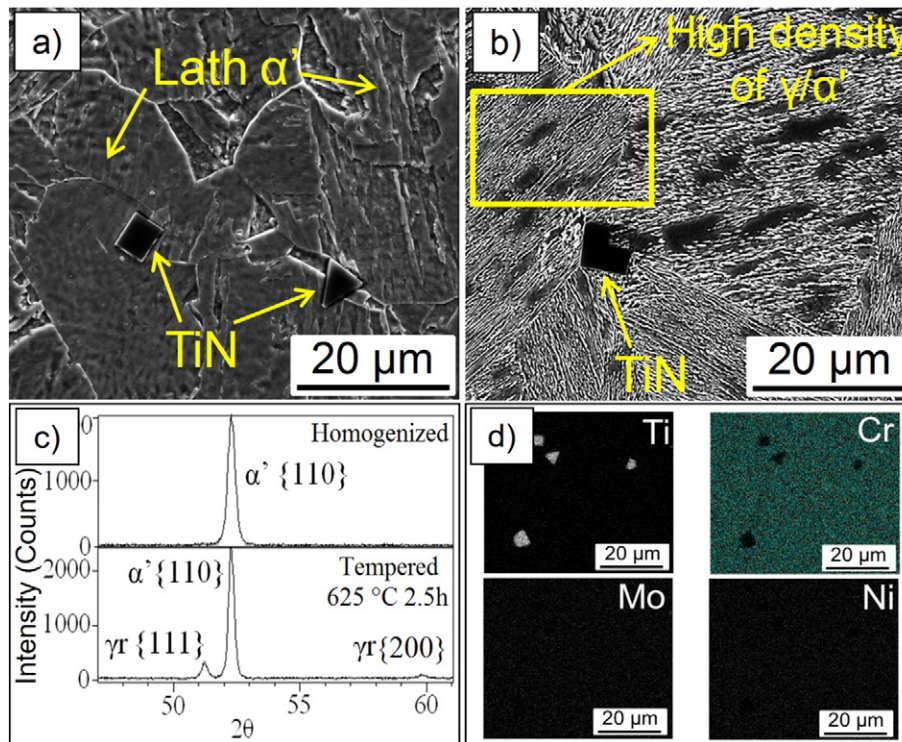


Fig. 2. Microstructural analysis of a Ti-stabilized SMSS after a) homogenization at 950 °C for 20 min, and b) furnace tempering at 625 °C for 2.5 h. c) X-ray diffraction analysis confirmed absence of retained austenite after homogenization (a) and presence of 0.19 volume fraction of γ_r after tempering (b). d) SEM-XEDS maps show the presence of angular TiN precipitates after homogenization.

gradient, the interface can be arbitrarily positioned within the 4 nm region between α' and γ_r , as represented by the light gray dashed squares in Figs. 5 and 6.

The chemical gradients across γ_{r1}/α' and γ_{r2}/α' interfaces show Cr, Si, Ti and Mo segregation within the 4 nm highlighted region. Negligible partitioning away from the interface was observed for Cr, Si and Ti, while slight enrichment of Mo was evidenced only in α' . To quantify such segregation tendency, enrichment factors were determined as the ratio between the atomic concentration peak at the interface and the core composition. Molybdenum showed the highest interface segregation tendency, followed by Si and Cr, respectively. These results are summarized in Table 3.

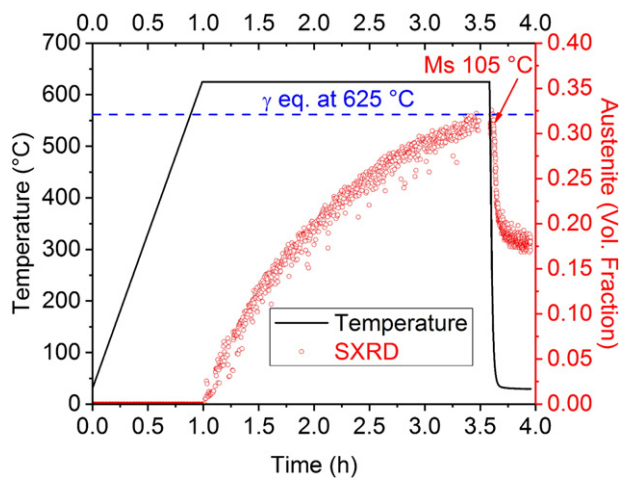


Fig. 3. Austenite transformation kinetics measured by SXR during the ICT cycle. Heating rate: 0.167 °C·s⁻¹, soaking temperature: 625 °C, soaking time: 2.5 h, cooling rate: 5 °C·s⁻¹. The blue dashed line indicates the equilibrium γ fraction at 625 °C.

Strong partitioning of Ni according to local equilibrium conditions is the primary cause for austenite stabilization at room temperature. Despite near equilibrium partitioning of Cu and Mn into γ_r , it is clear that these two elements play less important roles in austenite stabilization due to their small contribution to the nominal alloy composition.

The equilibrium compositions for γ , α and MCN calculated at 625 °C for two thermodynamic systems are shown in Table 4. The Ni concentration showed good agreement with the equilibrium calculations away from the γ_{r1}/α' interface. A 3:1 γ_r to α' Ni partitioning was observed, related to core compositions of 10.2 ± 0.01 and 3.4 ± 0.04 Ni at.% for γ_r and α' , respectively. For both the γ_{r1}/α' and γ_{r2}/α' interfaces, a progressive Ni depletion was observed from the martensite side towards the interface, with a minimum around 2.7 ± 0.02 at.% Ni, followed by a fast increase up to a peak value around 11.5 ± 0.2 at.%. This peak value is above the expected equilibrium calculations. Although both interfaces evidenced similar minimum and maximum Ni concentrations, the γ_{r2}/α' interface showed a steep Ni reduction towards γ_{r2} , reaching 8.1 ± 0.2 at.% of Ni.

Carbon did not participate directly in the austenite stabilization process, as neither partitioning nor interface segregation was observed. In fact, as described in detail later in Fig. 12, both γ_r and α' were found to be relatively carbon free due the precipitation of Ti (C, N). On the other hand, V partitioning was observed into the α' matrix. No VC precipitates were evidenced in the APT dataset, which is expected from the thermodynamic calculations. Preferential precipitation of Ti (C,

Table 2

Quantification of the austenite volume fraction for the in situ ($6\gamma + 5\alpha'$ peaks) and ex situ ($5\gamma + 4\alpha'$) conditions.

| Condition | Reverted austenite (Volume Fraction) |
|----------------------------|--------------------------------------|
| Equilibrium at 625 °C | 0.32 |
| High temperature (in situ) | 0.32 |
| Room temperature (in situ) | 0.20 |
| Room temperature (furnace) | 0.19 |

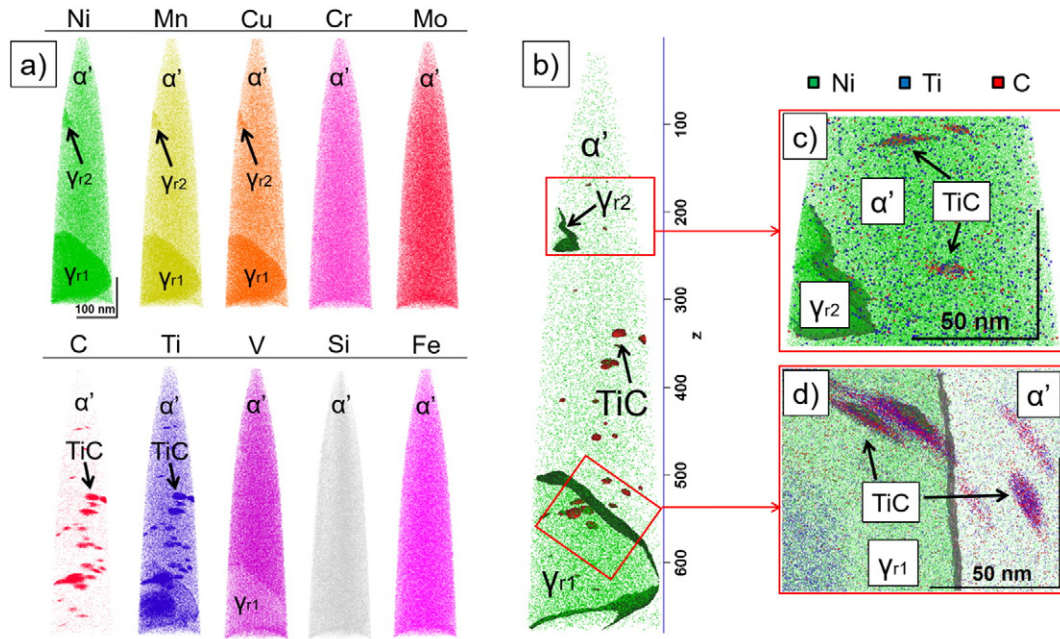


Fig. 4. a) APT tomographic reconstruction for the most representative alloying elements of the sample. b) Two reverted austenites (γ_{r1} and γ_{r2}) and several titanium carbides (TiC) defined by 6 at.% Ni and 30 at.% Ti + C isoconcentration surfaces, respectively. c) and d) are magnified regions of the γ_{r2}/α' and γ_{r1}/α' interfaces, respectively. Ni, Ti, and C atoms are shown as green, blue, red dots, respectively. Note that the TiC may have a deviated shape due to the local magnification effect resulting from the large difference in evaporation field between the TiC and the matrix material.

N) occurs when Ti is added to SMSS [40–42]. Titanium peaks were present not only at the interface, but also inside γ_f and α' matrixes. Nevertheless, the latter were associated to Ti (C, N) precipitation, as indicated by the black arrows in Fig. 6, and not to Ti partitioning.

Further STEM-XEDS compositional analysis, presented in Fig. 7a, showed good agreement with the APT measurements. Strong Ni partitioning into γ_f was evidenced. Whereas, no evidence of Cr or Mo

partitioning was seen. From the line compositional analysis performed along two austenite laths and crossing four γ_f/α' interfaces, it can be observed that the Ni concentration within γ_f tends to approach the equilibrium composition (10.7 at.%). Interestingly, regions of Ni concentration above (12 at.%) and below (9 at.%) the equilibrium were also observed, as depicted in Fig. 7b. This is consistent with the APT results in Fig. 5, where a 30 nm region with Ni enrichment above the equilibrium was

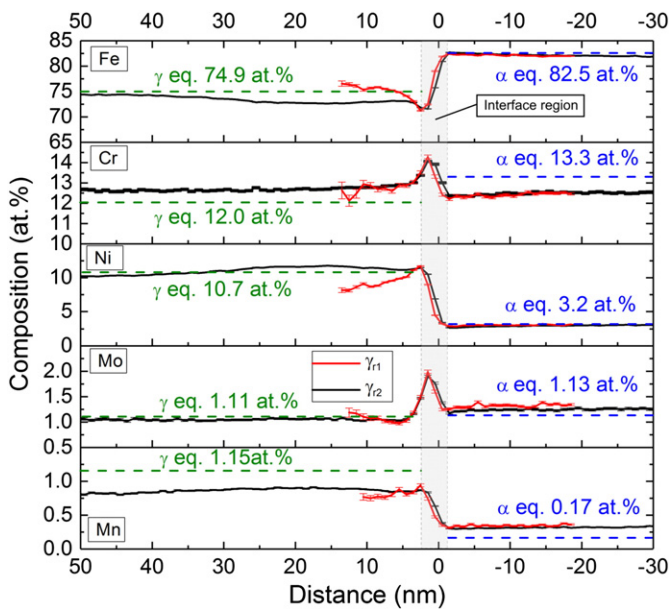


Fig. 5. Quantitative chemical analysis of Fe, Cr, Ni, Mo and Mn across the γ_1/α' (black) and γ_2/α' (red) interfaces shown in Fig. 4 after ICT cycle at 625 °C for 2.5 h. The dashed gray square represents the interface region, whereas distance 0 represents the 6% Ni isoconcentration surfaces used to perform the proximity histogram analysis. The blue and green horizontal dashed lines represent the ferrite and austenite equilibrium compositions, respectively.

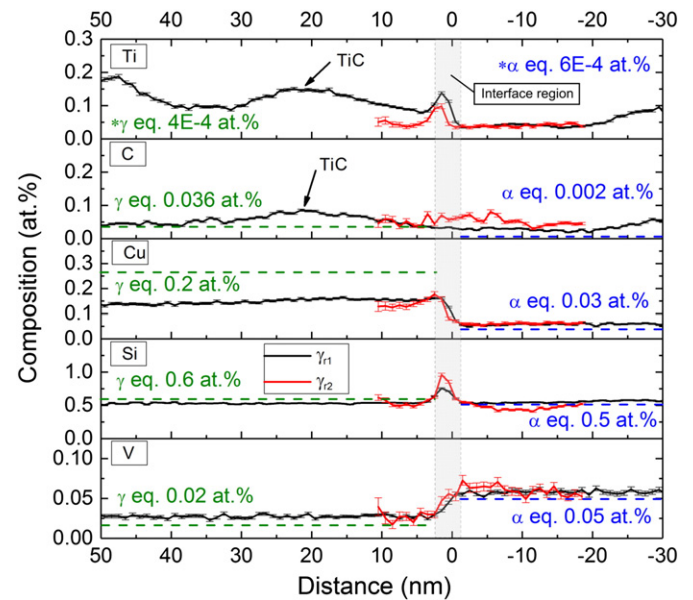


Fig. 6. Quantitative chemical analysis of Ti, C, Cu, Si and V across the γ_{r1}/α' (black) and γ_{r2}/α' (red) interfaces shown in Fig. 4 after ICT cycle at 625 °C for 2.5 h. The dashed gray square represents the interface region, whereas distance 0 represents the 6% Ni isoconcentration surfaces used to perform the proximity histogram analysis. The blue and green horizontal dashed lines represent the ferrite and austenite equilibrium compositions, respectively. * symbols in the Ti profile refer to compositions which are too small to plot.

Table 3

γ_r/α' interface segregation of ferrite-stabilizing elements. Compositions are given in atomic %s

| Element | Interface enrichment | γ -core | α' -core | Interface segregation (Peak/ γ -core) | Interface segregation (Peak/ α' -core) |
|---------|----------------------|----------------|-----------------|--|---|
| Mo | 1.90 | 1.03 | 1.30 | 1.84 | 1.46 |
| Si | 0.75 | 0.5 | 0.5 | 1.5 | 1.5 |
| Cr | 14.0 | 12.6 | 12.6 | 1.1 | 1.1 |

observed inside the austenite near the γ_r/α' interface. On the other hand, regions with Ni concentration profiles below the equilibrium, such as for the γ_{r2}/α' profile in Fig. 5, were also seen for the XEDS-STEM measurements. This suggests that the compositional equilibrium condition was not reached after 2.5 h of isothermal reversion.

Away from the γ_r laths, the Ni concentration in the matrix approached the equilibrium for α (3.2 at.%). Nonetheless, between two adjacent γ_r laths, the Ni concentration in the α' matrix was below the equilibrium for α . This is related to the fundamental role of Ni diffusion from α' to the moving interface at this temperature [24,25].

3.2.2. Matrix/Ti (C, N) interface

The averaged proximity histogram results for the 30 at.% Ti + C isoconcentration surfaces shown in Fig. 4b for the 7 precipitates in α' (red) and 5 precipitates in γ_r (black) are presented in Fig. 8. In both cases, rejection of Fe, Cr and Ni, and enrichment in C, Ti and Mo towards the core of the precipitates were observed. In order to conduct a more accurate compositional analysis, a peak deconvolution analysis was performed only for the ions contained inside the 30 at.% Ti + C isoconcentration surface. This was done in order to reduce the contribution of elements from the matrix present in the surroundings of the precipitates. Results are summarized in Fig. 9.

Negligible compositional differences were evidenced regardless the type of matrix. The precipitates were mainly composed by 38–40 at.% Ti, 36 at.% C and 16–17 at.% Mo with residual presence of Cr and Fe below 6 at.%, as well as traces of Ni and Mn below 1 at.%. Little presence of carbide forming elements, such as Nb and V was observed. Furthermore, no presence of N was detected using peak decomposition between Si and N. Although the precipitates are rather large, compositional error greater than the reported standard error is possible and can be associated with ion crossing from matrix regions into the carbides during field evaporation for the APT experiment. Ion crossing could cause the detected matrix element composition within the precipitate to be higher than the actual composition. In addition, complex field evaporation of carbides results in complex molecular evaporation and multiple evaporation events during one pulse, which can create error in the composition beyond the standard error presented [43–45]. However, overlapping peaks, such as $C2^+$, $C4^{++}$, and Ti^{+++} at 24 Da, were decomposed for the compositional measurements.

Fig. 10a shows STEM-XEDS compositional mapping of a region containing two nanometric precipitates, one at the γ_r/α' interface and other in the α' matrix. Both particles evidenced a significant enrichment of Ti, Mo, C, N and V when compared to the matrix. The line compositional

Table 4

Equilibrium composition for γ , α and MCN calculated at 625 °C for two thermodynamic systems.

| Phase | Fe | Cr | Cu | Mn | Mo | Ni | Si | Ti | V | C | N |
|--------------------------------|------|------|------|-----|-----|------|-----|---------|------|----------|----|
| a) All phases. Atomic %. | | | | | | | | | | | |
| γ | 74.9 | 11.7 | 0.2 | 1.2 | 0.7 | 10.6 | 0.6 | 4.6E-03 | 0.02 | 2.1E-03 | – |
| α | 82.5 | 12.8 | 0.03 | 0.2 | 0.7 | 3.3 | 0.5 | 7.6E-03 | 0.06 | 10.5E-03 | – |
| MCN | – | – | – | – | – | – | – | 50.8 | 0.02 | 31.2 | 18 |
| b) FCC and BCC only. Atomic %. | | | | | | | | | | | |
| γ | 74.2 | 12.0 | 0.2 | 1.2 | 1.1 | 10.7 | 0.6 | 4.0E-04 | 0.02 | 3.7E-02 | – |
| α | 81.5 | 13.3 | 0.03 | 0.2 | 1.1 | 3.2 | 0.5 | 6.4E-04 | 0.05 | 2E-03 | – |
| MCN | – | – | – | – | – | – | – | 50 | – | 33 | 17 |

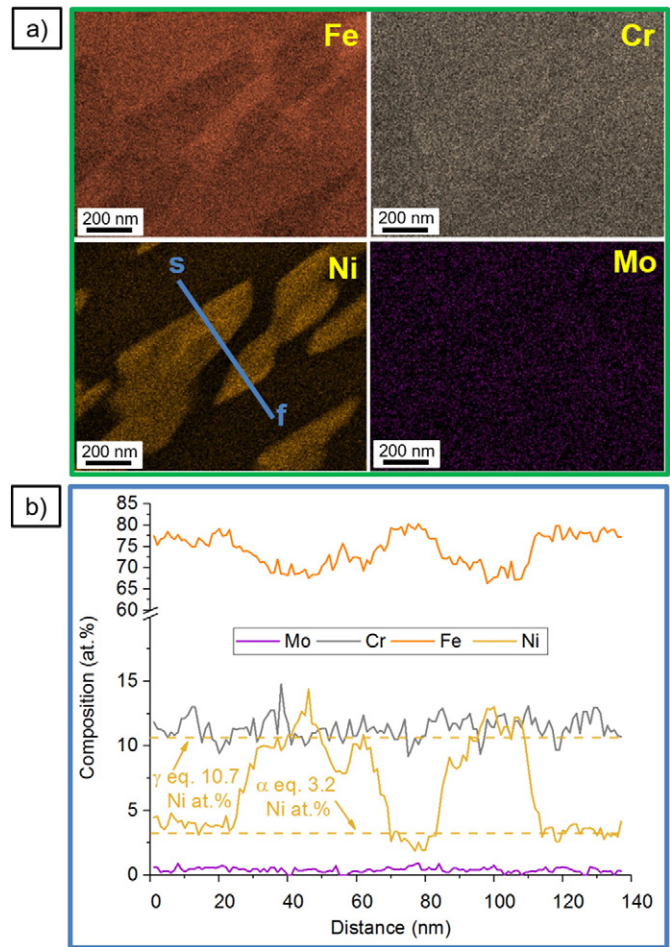


Fig. 7. a) STEM-XEDS compositional maps for Fe, Cr, Ni and Mo. b) Line compositional analysis for Fe, Cr, Ni and Mo through two γ_r laths. s: start; f: finish. The dashed lines represent the Ni equilibrium compositions for γ and α phases.

profile presented in Fig. 10b shows a similar trend when compared to the APT results shown in Fig. 8. Reduction in Fe, Cr and Ni, and increment in Ti and Mo were observed. However, the accurate determination of the composition of these small precipitates is hampered by the X-ray signal coming from the matrix above and/or below, as these do not extend across the whole thin foil thickness. Additionally, C and N were not taken into account for the chemical composition quantification due to the inherent limitations of XEDS to adequately quantify such light elements.

4. Discussion

4.1. Austenite reversion mechanism

There are three main mechanisms reported in the literature for the reversion of nano-sized austenite in Fe-Mn [11–13], Fe-Cr-C [16] and Fe-Cr-Ni-Mo [14,15] steels. First, interface-coherent allotropic austenite reversion with K-S orientation, which can occur at the α'/α' lath boundary aided by strong interface segregation of γ -stabilizing elements and the release of elastic stress from martensite [13,46]. The austenite growth is controlled by partitioning of γ -stabilizing elements at or near the equilibrium composition. Second, austenite can grow from previously existing reverted or retained austenite [14–16,28,34,47]. For example, in Mn diffusion controlled austenite reversion, the Mn composition of the newly formed austenite is imposed by local equilibrium at the particular reversion temperature. Therefore, the two austenitic phases can be distinguished by compositional differences, where the

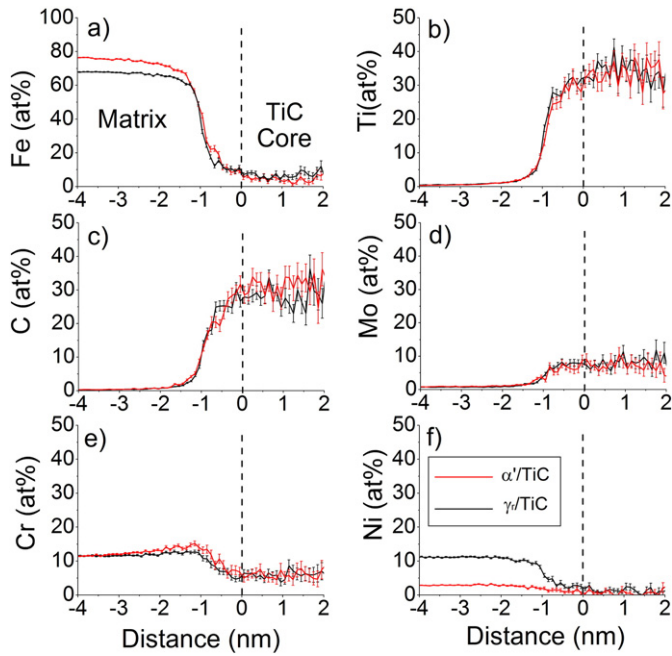


Fig. 8. Averaged proximity histograms of the Carbide/Matrix interface for 7 precipitates in α' (red) and 5 precipitates in γ_r (black). The analysis was performed using a 30 at.% Ti + C isoconcentration surface. The 0 value in the distance axis represents a 30 at.% Ti + C isoconcentration surface, and does not correlate to the exact position of the interface between the precipitates and the matrix.

retained austenite typically shows nominal alloy content of stabilizing elements [12,13]. Finally, nucleation of austenite can also be aided by the precipitation of carbides [5,6,14,15,27]. For example, the precipitation of $M_{23}C_6$ along the tempered martensite laths in a Fe-13Cr-4Ni-Mo can become heterogeneous nucleation sites for austenite reversion [14].

According to SXR measurements, no retained austenite was found in the homogenized condition before tempering. This is explained by the extreme hardenability of Fe-12Cr-6Ni-2Mo SMSS, which guarantees complete martensitic transformation after cooling from the austenitic field [48]. Additionally, according to Figs. 4 and 10, precipitation of TiC at the γ_r/α' interfaces was observed. As seen by APT, very low Ni remained in the precipitates. This can be beneficial for austenite reversion at regions with a high density of precipitation, since nucleation of austenite is more probable in regions with higher local concentrations of Ni. Nevertheless, the volume fraction of MCN is very small (below 0.003 volume fraction at 625 °C), and this effect is not expected to be

fundamental for the reversion mechanism. Therefore, the reversion mechanism studied in this work can be associated mainly to α'/α' lath boundary segregation of γ -stabilizing elements, followed by nucleation and growth of austenite, mainly controlled by the local equilibrium partitioning of Ni at the reversion temperature.

4.2. Austenite stabilization mechanism

According to kinetic calculations, the austenite initially nucleates with a nucleus composition of 61.7 at.% Fe, 9.0 at.% Cr, 22.5 at.% Ni, 2.2 at.% Mo and 4.6 at.% Mn. During the isothermal growth, depicted in Fig. 11, the γ_r/α' interface advances according to the equilibrium Ni composition given by the tie-lines for a Fe - 12.8 at.%, Cr - 5.6 at.%, Ni - 1.1 at.%, Mo - 0.5 at.% Mn system. In the early stages of γ growth, an inhomogeneous Ni compositional profile inside γ is expected due to the gradient between the Ni-rich nuclei and the advancing interface. Also, the Ni diffusion from the matrix to the interface generates a local depletion near the interface related to the nominal Ni content. For longer isothermal reversion times, the interface continues to advance mainly due to Ni diffusion from the matrix, extending the size of the Ni depleted region between the interface and the nominal composition. According to Niessen et al., the isothermal austenite reversion of a 15Cr SMSS at 635 °C mainly depends on the diffusion of Ni from the tempered martensite matrix to the interface [24]. Whereas, for tempering temperatures above 700 °C, the reversion kinetics depends on the diffusivity of Ni in γ due to compositional homogenization. By the end of the isothermal stabilization process, the compositional profile inside γ is mostly homogenized according to the local equilibrium of austenite (dashed line). The γ growth decelerates due to the exhaustion of Ni in the matrix, which approaches the local equilibrium composition for α (dotted line). This is consistent with the measurements presented in Fig. 5.

Nonetheless, an inhomogeneous Ni distribution inside γ_r was experimentally observed by APT and STEM-XEDS. This can be related to several factors, such as the lack of homogenization at the Ni-rich regions where γ nucleated, the nucleation sequence, and to further Ni enrichment upon cooling. The latter can become relevant for the present case due to the slow furnace cooling rate, as the solubility of Ni in γ increases for lower temperatures [23–25].

Chromium partitioning into α is also expected to occur as the interface advances according to the equilibrium tie-lines. Nonetheless, APT observations evidenced that negligible partitioning is obtained away from the interface, although it advances with a strong Cr segregation. According to Fig. 5, a slight Cr enrichment is left within the first 30 nm inside γ_r ; whereas, a slight Cr depletion within a similar distance is evidenced in α' . Chromium partitioning into γ_r was reported by other authors for the specific case of a tempered SMSS [14]. However, this result is most likely related to a size effect, since the compositional profile was measured only across 10 nm away from the interface.

The effect of Mo is not expected to be significant as the difference in equilibrium partitioning between γ_r and α' is less than 0.02 at.% for the two thermodynamic systems in Table 4. It is interesting to note that, for the Fe - 12.8 at.%, Cr - 5.6 at.%, Ni - 1.1 at.%, Mo - 0.5 at.% Mn composition used for the kinetic modeling, Mo is expected to partition into γ_r . Nonetheless, this discrepancy with the APT observations is related to the simplification of the nominal composition.

Even though high temperature microstructural equilibrium was confirmed by SXR, it is likely that 9000 s (2.5 h) of isothermal reversion at 625 °C is not enough to homogenize all compositional gradients inside γ_r , especially for the laths that nucleated near the end of the isothermal stage. Regions with Ni partitioning as small as 8.1 ± 0.2 at.%, such as γ_{r2} in Fig. 5, were observed. As the γ_r thermal stability greatly depends on the degree of Ni partitioning, it is expected that the less Ni-enriched regions will be more susceptible to $\gamma_r \rightarrow \alpha'$ transformation upon cooling, as observed in Fig. 3. Nevertheless, such freshly formed Ni-rich martensite laths will become preferential sites for eased austenite reversion during multi-stage ICT cycles [5,25,34,47,49].

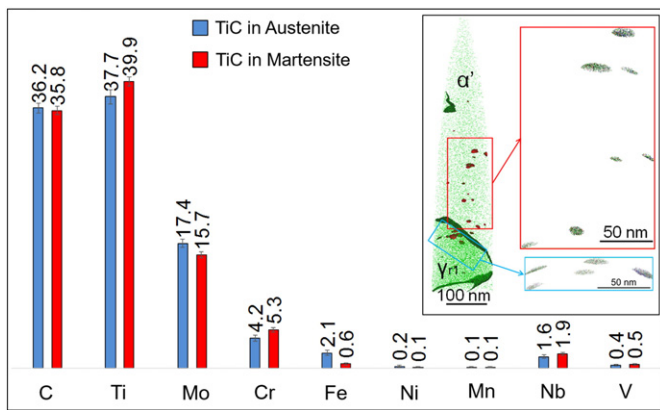


Fig. 9. Average composition of titanium carbides in α' and γ_r . Peak deconvolution analysis was conducted using a 30 at.% Ti + C isoconcentration surface in order to minimize matrix contributions. Local range-assisted background correction.

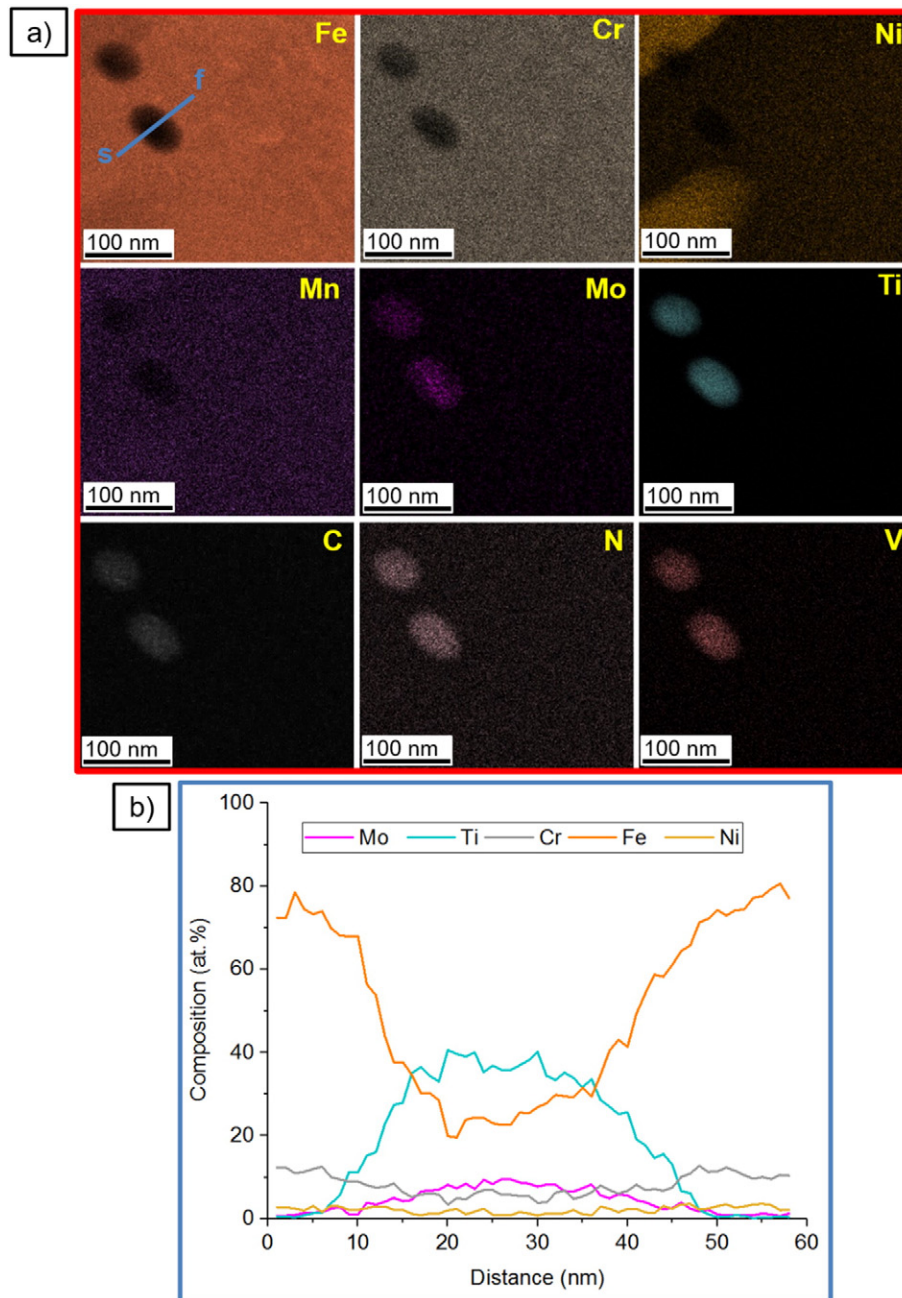


Fig. 10. a) STEM-XEDS compositional maps for the main alloying elements in the system. b) Line compositional analysis through a nanometric Ti-rich particle. s: start; f: finish. STEM-XEDS and APT results differ due to the matrix interference during the XEDS analysis.

4.3. Role of carbide precipitation and carbon content

For the specific case of low carbon martensitic stainless steels, a wide variety of nanometric precipitates, such as $M_{23}C_6$, M_7C_3 , M_3C , M_2C , MCN and VN have been found at room temperature after heat treatments or welding cycles [5,6,14,25,27,34,40,50]. However, when titanium is added to SMSS, the precipitation of MCN is preferred over any other type of carbide [40–42]. The most relevant secondary phases at the tempering temperature of 625 °C, for a thermodynamic calculation allowing all possible phases, are MCN, $M_{23}C_6$ and χ . Nevertheless, no experimental evidence of the precipitation of $M_{23}C_6$ and χ was observed after 2.5 h of isothermal reversion. Therefore, the most reasonable candidate for the precipitates observed in Fig. 9 is MCN, or Ti (C, N), with partial substitution of Ti by Mo. Despite the presence of Cr, and Fe was also

observed by ATP, the hypothesis of matrix contamination due to differences in evaporation rate cannot be disregarded, but it is highly probable that these elements exist in the precipitates due to their large size. Transmission electron microscopy characterization of TiC carbides in Ti-stabilized 12.7Cr SMSS showed that Cr, Mo and Si can also be present as small quantities [40]. Additionally, it has been reported that incorporation of Mo seems to favor TiC nucleation through the reduction of the interfacial energy between TiC and the austenitic matrix [51]. Although N was clearly identified using STEM-XEDS, it is challenging to accurately quantify the concentration of N in Ti (C, N) due to peak overlap between N and Si in APT, and to the small nominal content of N in the steel. However, there was not a significant amount of N in the Ti (C, N), as indicated by the number of counts in the 28 Da peak compared to the 29 and 30 Da peaks, which matched the isotopic abundance of Si.

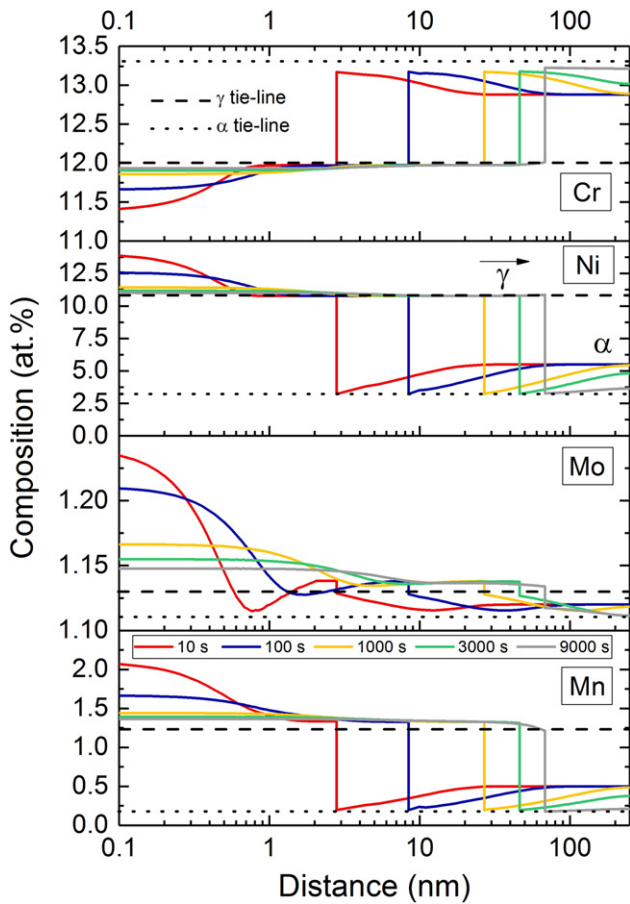


Fig. 11. Simulation of the isothermal austenite reversion kinetics and elemental partitioning calculated at 625 °C for several transformation times. The austenite grows in the ferritic matrix from the left to the right.

The average carbonitride composition was found to be very similar, regardless of the matrix in which these were found. These similarities can be a consequence of a fast precipitation in the α' matrix and at the α'/α' lath interfaces before significant austenite reversion takes place. It has been reported that MCN can precipitate even during the first minutes of the austenite reversion during tempering of SMSS [52].

In order to clarify the role of Ti and C in the austenite reversion mechanism, local peak deconvolution analyses were conducted in regions away from the interface with no presence of precipitates. The content of Ti within the γ_{r1} core (0.2 at.%) and within the α' matrix (0.04 at.%) were above the equilibrium predictions. Whereas, both γ_r and α' phases were virtually carbon-free, as evidenced by the absence of C peaks in the mass spectrum plot. Compositional results are summarized in Fig. 12. Although the γ_{r1} austenite lath core was rich in Ti, no additional C, Cr or Mo enrichment was observed. Therefore, this local enrichment is related neither to partitioning, nor to the presence of MCN, $M_{23}C_6$, or χ phases. This local Ti-rich region may be associated to carbide dissolution and insufficient homogenization of Ti during the austenitization stage at 950 °C. Although this region could be associated to a nucleation site for γ_r , further characterization of a larger number of γ_r laths by APT is necessary to carefully address this issue. The overall presence of Ti above the equilibrium in γ_r and α' , and the partitioning of V into α' can be related to the lack of C in solid solution to produce further carbide precipitation.

5. Conclusions

The mechanism for austenite reversion and stabilization during inter-critical tempering at 625 °C of a Ti-stabilized supermartensitic stainless steel was studied using atom probe tomography, scanning transmission electron microscopy, energy dispersive X-ray spectroscopy, synchrotron X-ray diffraction, and thermodynamic and kinetic calculations. The most relevant conclusions are as follows:

- The austenite reversion mechanism was associated to nucleation and growth at the α'/α' lath interface assisted by the precipitation

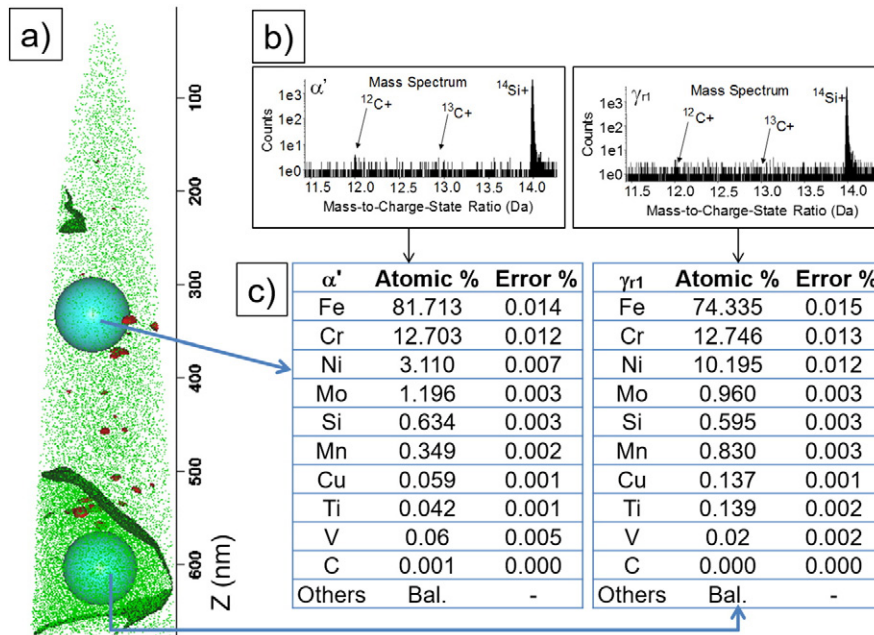


Fig. 12. ROI compositional analysis of γ_{r1} and α' excluding the Ti-rich precipitates. b) Mass Spectrum evidencing carbon free martensite and austenite. c) IVAS peak deconvolution analysis. Local range-assisted background correction.

of Ti (C, N). Interfacial segregation of ferrite stabilizing elements (Cr, Mo, Si and Ti) was found at the γ/α' interface after tempering. Nevertheless, austenite growth occurred only by partitioning of austenite stabilizing elements (Ni, Mn and Cu). Negligible partitioning of Cr and Si was observed away from the interfaces.

- The mechanism behind the austenite stabilization in Ti-stabilized SMSS was mainly related to strong partitioning of Ni according to the local equilibrium at 625 °C, and was independent of C. The austenite growth was controlled by Ni diffusion from the martensitic matrix. The kinetics slowed down as the Ni was exhausted within the surrounding tempered martensite, approaching the local equilibrium for ferrite.
- Even though high temperature microstructural equilibrium was confirmed by synchrotron X-ray diffraction, it was observed that 9000 s (2.5 h) of isothermal reversion at 625 °C was not enough to achieve compositional equilibrium. This was evidenced by the partial martensitic transformation observed upon cooling. Nonetheless, this inter-critical tempering cycle reduced the hardness from 308 ± 7 to 286 ± 6 HV, which is a typical value for tempered SMSS pipes for applications in the oil and gas industry.
- Carbon and titanium played a secondary role in the austenite stabilization mechanism through the precipitation of Ti (C, N). Virtually carbon-free austenite and martensite were observed away from the interfaces and precipitates.

Acknowledgements

The authors acknowledge the XTMS beamline members, the Brazilian Synchrotron Light Source (LNLS) and the Brazilian Nanotechnology National Laboratory (LNNano) for the support with the diffraction experiments; Villares Metals S.A. for the donation of the materials; and CNPq-SWE 02766/2014-4, FAPESP (2014/20844-1), FAPESP (2016/13466-6) for the PhD funding. APT was conducted at ORNL's Center for Nanophase Materials Sciences (CNMS), which is a U.S. DOE Office of Science User Facility. FIB and TEM measurements were performed at the Center for Electron Microscopy and Analysis (CEMAS), at The Ohio State University.

References

- [1] X.P. Ma, L.J. Wang, C.M. Liu, S.V. Subramanian, Microstructure and properties of 13Cr5Ni1Mo0.025Nb0.09V0.06N supermartensitic stainless steel, *Mater. Sci. Eng. A* 539 (2012) 271–279.
- [2] G.F. Silva, S.S.M. Tavares, J.M. Pardal, M.R. Silva, H.F.G. Abreu, Influence of heat treatments on toughness and sensitization of a Ti-alloyed Supermartensitic stainless steel, *J. Mater. Sci.* 46 (2011) 7737–7744.
- [3] D. Xu, Y. Liu, Z. Ma, H. Li, Z. Yan, Structural refinement of 00Cr13Ni5Mo2 supermartensitic stainless steel during single-stage intercritical tempering, *Int. J. Miner. Metall. Mater.* 21 (2014) 279–288.
- [4] Ye Dong, Li Jun, Jiang Wen, Su Jie, Zhao Kunyu, Effect of Cu addition on microstructure and mechanical properties of 15%Cr super martensitic stainless steel, *Mater. Des.* 41 (2012) 16–22.
- [5] M. Sanctis, G. Lovivu, R. Valentini, A. Dimatteo, R. Ishak, U. Migliaccio, R. Montanari, E. Pietrangeli, Microstructural features affecting tempering behaviour of 16Cr-5Ni Supermartensitic steel, *Metall. Mater. Trans. A* 46A (2015) 1878–1887.
- [6] X.-H. W-H Yuan, Y.-Q. Gng, J.-X. Sun, Liang, Microstructure evolution and precipitation behavior of 0Cr16Ni5Mo martensitic stainless steel during tempering process, *J. Iron Steel Res. Int.* 23 (2016) 401–408.
- [7] M. Karlson, Ø. Grong, M. Sofferud, J. Hjelen, G. Rørvik, R. Chiron, Scanning electron microscopy/electron backscatter diffraction based observations of Martensite variant selection and slip plane activity in Supermartensitic stainless steels during plastic deformation at elevated, ambient, and subzero temperatures, *Metall. Mater. Trans. A* 40 (2009) 310–320.
- [8] M. Karlson, J. Hhelen, Ø. Grong, G. Rørvik, R. Chiron, U. Schubert, E. Nilsen, SEM/EBSD based in situ studies of deformation induced phase transformations in Supermartensitic stainless steels, *Mater. Sci. Technol.* 24 (2008) 64–72.
- [9] N.H. Dijk, A.M. Butt, L. Zhao, J. Sietsma, S.E. Offerman, J.P. Wright, S. Zwaag, Thermal stability of retained austenite in TRIP steels studied by synchrotron X-ray diffraction during cooling, *Acta Mater.* 53 (2005) 5439–5447.
- [10] P.J. Jacques, J. Ladrière, F. Delannay, On the influence of interactions between phases on the mechanical stability of retained austenite in transformation-induced plasticity multiphase steels, *Metall. Mater. Trans. A* 32A (2001) 2759–2768.
- [11] M. Kuzmina, M. Herbig, D. Ponge, S. Sandlöbes, D. Raabe, Linear complexes: Confined chemical and structural states at dislocations, *Science* 349 (2015) 1080–1083.
- [12] O. Dmitrieva, D. Ponge, G. Inden, J. Millán, P. Choi, J. Sietsma, D. Raabe, Chemical gradients across phase boundaries between martensite and austenite in steel studied by atom probe tomography and simulation, *Acta Mater.* 59 (2011) 364–374.
- [13] D. Raabe, S. Sandlöbes, J. Millán, D. Ponge, H. Assadi, M. Herbig, P.P. Choi, Segregation engineering enables nanoscale martensite to austenite phase transformation at grain boundaries: a pathway to ductile martensite, *Acta Mater.* 61 (2013) 6132–6152.
- [14] Y.Y. Song, D.H. Ping, F.X. Yin, X.Y. Li, Y.Y. Li, Microstructural evolution and low temperature impact toughness of a Fe-13Cr-4%Ni-Mo martensitic stainless steel, *Mater. Sci. Eng. A* 527 (2010) 614–618.
- [15] Y.Y. Song, X.U. Li, L.J. Rong, D.H. Ping, F.X. Yin, Y.Y. Li, Formation of the reversed austenite during intercritical tempering in a Fe-13Cr-4%Ni-Mo martensitic stainless steel, *Mater. Lett.* 64 (2010) 1411–1414.
- [16] L. Yuan, D. Ponge, J. Wittig, P. Choi, J.A. Jiménez, D. Raabe, Nanoscale austenite reversion through partitioning, segregation and kinetic freezing: example of a ductile 2GPa Fe-Cr-C steel, *Acta Mater.* 60 (2012) 2790–2804.
- [17] Y. Liu, Y. Dong, Q.L. Yong, J. Su, K.Y. Zhao, W. Jiang, Effect of heat treatment on microstructure and property of Cr13 supermartensitic stainless steel, *J. Iron Steel Res. Int.* 18 (2011) 60–66.
- [18] D. Zou, Y. Han, W. Zhang, X. Fang, Influence of tempering process on mechanical properties of 00Cr13Ni4Mo Supermartensitic stainless steel, *J. Iron Steel Res. Int.* 17 (2010) 50–54.
- [19] K. Kondo, H. Amaya, T. Ohmura, K. Moriguchi, Effect of cold work on retained austenite and on corrosion performance in low carbon martensitic stainless steels, *Corrosion* 2003. Paper 0394, 2003 (Houston, Texas).
- [20] D. Leem, Y. Lee, J. Jun, C. Choi, Amount of retained austenite at room temperature after reverse transformation of Martensite to austenite in an Fe-13Cr-7%Ni-3%Si martensitic stainless steel, *Scr. Mater.* 45 (2001) 767–772.
- [21] L. Liu, Z.G. Yang, C. Zhang, W.B. Liu, An in situ study on austenite memory and austenitic spontaneous recrystallization of a martensitic steel, *Mater. Sci. Eng. A* 527 (2010) 7204–7209.
- [22] J. Enerhaug, Ø. Grong, U.M. Steinsmo, Factors affecting initiation of pitting corrosion in supermartensitic stainless steel weldments, *Sci. Technol. Weld. Join.* 6 (2001) 330–338.
- [23] J.D. Escobar, G.A. Faria, L. Wu, J.P. Oliveira, P.R. Mei, A.J. Ramirez, Austenite reversion kinetics and stability during tempering of a Ti-stabilized supermartensitic stainless steel: correlative in situ synchrotron X-ray diffraction and dilatometry, *Acta Mater.* 138 (2017) 92–99.
- [24] F. Niessen, M. Villa, J. Hald, M.A.J. Somers, Kinetics analysis of two-stage austenitization in supermartensitic stainless steel, *Mater. Des.* 116 (2017) 8–15.
- [25] L. Bojack, P.F. Zhao, J. Morris, Sietsma, in-situ determination of austenite and Martensite formation in 13Cr6Ni2Mo supermartensitic stainless steel, *Mater. Charact.* 71 (2012) 77–86.
- [26] Y.K. Lee, H. Shin, D. Leem, J. Choi, W. Jin, C. Choi, Reverse transformation mechanism of martensite to austenite and amount of retained austenite after reverse transformation in Fe-3Si-13Cr-7Ni (wt-%) martensitic stainless steel, *Mater. Sci. Technol.* 19 (2003) 393–398.
- [27] S. Zhang, P. Wang, D. Li, Y. Li, Investigation of the evolution of retained austenite in Fe-13Cr-4%Ni martensitic stainless steel during intercritical tempering, *Mater. Des.* 84 (2015) 385–394.
- [28] W. Jiang, D. Ye, J. Li, J. Su, K. Zhao, Reverse transformation mechanism of Martensite to austenite in 00Cr15Ni7Mo2Wc2 super martensitic stainless steel, *Steel Res. Int.* 85 (2013) 1150–1156.
- [29] S.J. Lee, J.M. Park, Y.K. Lee, Reverse transformation mechanism of martensite to austenite in a metastable austenitic alloy, *Mater. Sci. Eng. A* 515 (2009) 32–37.
- [30] F.G. Caballero, M.K. Miller, S.S. Babu, C. Garcia-Mateo, Atomic scale observations of bainite transformation in a high carbon high silicon steel, *Acta Mater.* 55 (2007) 381–390.
- [31] F.G. Caballero, M.K. Miller, C. Garcia-Mateo, Carbon supersaturation of ferrite in a nanocrystalline bainitic steel, *Acta Mater.* 58 (2010) 2338–2343.
- [32] H.S. Park, J.C. Han, N.S. Lim, J.B. Seol, C.G. Park, Nano-scale observation on the transformation behavior and mechanical stability of individual retained austenite in CMnSiAl TRIP steel, *Mater. Sci. Eng. A* 627 (2015) 262–269.
- [33] M. Herbig, M. Kuzmina, C. Haase, R.K.W. Marceau, I. Gutierrez-Urrutia, D. Haley, D.A. Molodov, P. Cho, D. Raabe, Grain boundary segregation in Fe-Mn-C twinning-induced plasticity steels studied by correlative electron backscatter diffraction and atom probe tomography, *Acta Mater.* 83 (2015) 37–47.
- [34] P.D. Bilmes, M. Solari, C.L. Llorente, Characteristics and effects of austenite resulting from tempering of 13Cr-NiMo martensitic steel weld metals, *Mater. Charact.* 46 (2001) 285–296.
- [35] G.A. Faria, Exploring Metallic Materials Behavior through in Situ Crystallographic Studies, State University of Campinas, 2014.
- [36] M.K. Miller, Atom Probe Tomography: Analysis at the Atomic Level, Springer US, 2000.
- [37] C.M. Garzon, A.J. Ramirez, Growth kinetics of secondary austenite in the welding microstructure of a UNS S32304 duplex stainless steel, *Acta Mater.* 54 (2006) 3321–3331.
- [38] M. Wiessner, E. Gamsjäger, S. van der Zwaag, P. Angerer, Effect of reverted austenite on tensile and impact strength in a martensitic stainless steel – an in-situ X-ray diffraction study, *Mater. Sci. Eng. A* 682 (2017) 117–125.
- [39] G. Stechauner, E. Kozeschnik, Assessment of substitutional self-diffusion along short-circuit paths in Al, Fe and Ni, *Calphad* 47 (2014) 92–99.
- [40] E. Ladanova, J.K. Solberg, T. Rogne, Carbide precipitation in HAZ of multiphase welds in titanium containing and titanium free supermartensitic stainless steels part 1 – proposed precipitation mechanisms, *Corros. Eng. Sci. Technol.* 41 (2006) 143–152.

- [41] C.A.D. Rodrigues, P.L.D. Lorenzo, A. Sokolowski, C.A. Barbosa, J.M.D.A. Rollo, Titanium and molybdenum content in supermartensitic stainless steel, *Mater. Sci. Eng. A* 460–461 (2007) 149–152.
- [42] E. Ladanova, J.K. Solberg, T. Rogne, Carbide precipitation in HAZ of multipass welds in titanium containing and titanium free supermartensitic stainless steels part 2 – weld simulation studies, *Corros. Eng. Sci. Technol.* 41 (2006) 152–160.
- [43] H.S. Kitaguchi, S. Lozano-Perez, M.P. Moody, Quantitative analysis of carbon in cementite using pulsed laser atom probe, *Ultramicroscopy* 147 (2014) 51–60.
- [44] Y.J. Li, P. Choi, C. Borchers, S. Westerkamp, S. Goto, D. Raabe, Atomic-scale mechanisms of deformation-induced cementite decomposition in pearlite, *Acta Mater.* 59 (2011) 3965–3977.
- [45] W. Sha, L. Chang, G.D.W. Smith, L. Cheng, E.J. Mittemeijer, Some aspects of atom-probe analysis of Fe-C and Fe-N systems, *Surf. Sci.* 266 (1992) 416–423.
- [46] S.H. Mun, M. Watanabe, X. Li, K.H. Oh, D.B. Williams, H.C. Lee, Precipitation of austenite particles at grain boundaries during aging of Fe-Mn-Ni steel, *Metall. Mater. Trans. A* 33A (2002) 1057–1067.
- [47] L. Couturier, F. De Geuser, M. Descoins, A. Deschamps, Evolution of the microstructure of a 15-5PH martensitic stainless steel during precipitation hardening heat treatment, *Mater. Des.* 107 (2016) 416–425.
- [48] K. Kondo, M. Ueda, K. Ogawa, H. Amaya, H. Hirata, H. Takabe, Alloy Design of Super 13 Cr Martensitic Stainless Steel (Development of Super 13 Cr Martensitic Stainless Steel for Line Pipe), *Supermartensitic Stainless Steels*, 99, 1999, pp. 11–18 (Belgium).
- [49] A. Bojack, L. Zhao, P.F. Morris, J. Sietsma, Austenite Formation from Martensite in a 13Cr6Ni2Mo Supermartensitic Stainless Steel, *Metall. Mater. Trans. A* 47A (2016) 1996–2009.
- [50] D. Carrouge, H.K.D.H. Bhadeshia, P. Woollin, Effect of δ -ferrite on impact properties of supermartensitic stainless steel heat affected zones, *Sci. Technol. Weld. Join.* 9 (2004) 377–389.
- [51] Z. Wang, H. Zhang, C. Guo, W. Liu, Z. Yang, X. Sun, Z. Zhang, F. Jiang, Effect of molybdenum addition on the precipitation of carbides in the austenite matrix of titanium micro-alloyed steels, *J. Mater. Sci.* 51 (2016) 4996–5007.
- [52] Sømme, Secondary Hardening in Two Supermartensitic Stainless Steels, Norwegian University of Science and Technology, 2012.